Hindawi
International Journal of Aerospace Engineering
Volume 2022, Article ID 9258503, 16 pages
https://doi.org/10.1155/2022/9258503

Research Article

Theoretical and Experimental Study on Rapid Decompression Oscillation in Altitude Chamber

Zifeng Tian,[1] **Jianfeng Lu**,[1] **Zhao Gu**,[2] **Lihua Yu**,[2] **Hao Zhou**,[1] **and Lijun Yang**[3]

[1]*College of Mechanical Engineering, Guizhou University, Guizhou, China*
[2]*Air Force Characteristic Medical Center of PLA Air Force Medical University, Air Force Medical University, Beijing, China*
[3]*Guizhou Fenglei Aviation Ordnance Co., Ltd, Guizhou, China*

Correspondence should be addressed to Jianfeng Lu; jflu@gzu.edu.cn

Received 27 August 2022; Revised 5 November 2022; Accepted 7 November 2022; Published 18 November 2022

Academic Editor: Jinchao Chen

Given the frequent airflow excitation phenomenon caused by the rapid decompression of the altitude chamber, the mathematical model of the nonlinear system of the rapid decompression of the altitude chamber is established. The polynomial parameter method is used to evaluate the characteristics of airflow oscillation, and a rapid decompression test system is built. The test results verify the pressure oscillation phenomenon of the numerical simulation. This paper proves the phenomenon of fluid-induced vibration in the process of rapid decompression and determines that the main factors affecting the induced oscillation are the diameter of the pipe (throat), pressure difference between the two chambers, and initial pressure conditions. Specifically, this study establishes safety and reliability for preventing engineering accidents caused by resonance in the altitude chamber.

1. Introduction

An altitude chamber is an experimental chamber that can simulate high-altitude and low-pressure environments. Its main purpose is to meet the needs of aviation equipment experimental identification, aviation medical research, and special physical training. Rapid depressurization refers to the process of artificial simulation of sudden failure or damage of high-altitude aircraft. The high-pressure gas in the chamber is rapidly discharged outward, resulting in a sharp decrease in the pressure in the aircraft. It is used to simulate instantaneous self-pressurization of the chamber to the thin atmospheric environment and the thin to the dense atmospheric environment during the landing process. The decompression process is a simulation type of a high-altitude environment. It is used for flight attendants, astronauts, and high-altitude operators to conduct high-altitude endurance inspections, hypoxia endurance inspections, high-altitude physiological training, high-altitude blasting training, and experimental identification of specific functional equipment in the composite environment chamber group [1–3]. Meanwhile, Lu et al. [4] made a reasonable analysis of the rapid decompression time in the research of the rapid decompression system of the altitude chamber; they used fluent to simulate and analyze the airflow balance process and dynamic simulation of the rapid decompression system, deduced the airflow balance equation, and proposed that the rapid decompression time of the altitude chamber is related to such factors as pipeline conductivity, initial pressure, pressure difference, and volume of altitude and vacuum chambers.

Rapid decompression of the line is an extremely dangerous process [5]. In the rapid decompression process, an inertial force appears when gas molecules flow through the pipeline under pressure balance. The fluid's initial state is the turbulent state. With the reduction of the pressure difference, the inertial force will gradually become weak. At this time, the friction force plays a major role in the internal gas, and the gas flow will also become a viscous flow state [6]. However, the precision of the friction for the transient unstable complicated fluid flow is poor, with high calculation quantity. Recently, Urbanowicz revised the unstable recurrence formula of unsteady wall shear stress in transient

flow in a study of the friction force of the liquid transient flow in tubes. He verified the accuracy of the effective weighting function obtained in the wall shear stress model, improved the transient flow calculation model using an effective weighting function, and expressed the best weighting function by using the fewest exponential terms. He also improved the numerical calculation speed and accuracy [7]. Pressure oscillations will occur during a quick decompression process, causing resonance in the pipe. The flow velocity will change with unstable fluid flow. Different pipe diameters, cross-sectional areas, and flow velocities will cause varying degrees of damage to transmission pipelines in the field of fluid pipeline transportation engineering [8], resulting in considerable economic losses [9]. The phenomenon of fluid pipeline resonance has become an important research object in the engineering field [10–12].

In fluid and engineering applications, fluid oscillation is always a major issue involving safety. In the case of consuming huge financial and material resources, we can only establish the database of some tests, so as to obtain the technical data of some tests. The parametric polynomial approach is essential in the field of complicated flow, particularly in fluid machinery [13], blade vibration of aerospace turbomachinery [14], maritime transportation engineering [15, 16], and other vital engineering applications. Through analysis of the chamber model, the numerical analysis method of the fluid distribution that is suitable for the rapid decompression of the altitude chamber is determined. Further, the velocity and pressure distributions in the pipeline under different conditions are determined.

Researchers investigating incompressible fluid vibration have created deterministic control equations and mathematical models for the analysis of the vibration of fluid transmission pipelines, aiding in the growth of the field [17–20]. For example, Bourrieres determined the control differential equation of fluid vibration in the analysis of a liquid transmission pipeline through a combination of experiments and theory [21]. Bhatti et al. considered transverse magnetic and axial electric fields and used the improved Darcy–Brinkman–Forchheimer model to establish mathematical models of laminar flow. They fully developed the viscoelastic natural convection electromagnetic hydrodynamics flow in microchannel systems containing air, thereby promoting the development of non-Newtonian heat treatment [22].

A study on free vibration of cylindrical shells with compressible fluid flow has been widely conducted [23–27]. Fluid vibration caused by the rapid decompression mainly occurs at the connecting pipe (throat) of two chambers. With the rapid movement of the airflow, the pressure difference becomes smaller, and the airflow state changes, forming a complex and variable nonlinear system. In recent years, in a study of fluid nonlinear systems, Skrickij et al. [28] used several physical models to investigate the influence of cavitation on the performance of a single-tube shock absorber. When the shock absorber is running at high speeds, the cavitation effect occurs. The damping force when the cavitation effect occurs is determined by the inner diameter of the absorber and starting pressure. The fluid will vibrate if the flow medium route shrinks. However, long-term vibration will impair the shock absorber's performance. Massoudi and Vaidya [29] investigated the unsteady motion of nonuniform incompressible viscous fluid with viscosity varying with space. They obtained the flow results between two parallel plates (one of which has an oscillation phenomenon). This result establishes the exact solution of a large class of unsteady nonlinear problems, which will obtain the exact solution in stable systems. However, no exact solutions exist for many nonlinear systems. For example, the rapid decompression system of a low-pressure chamber, which is the object of this paper, will oscillate; thus, this exact solution does not exist.

Literature [30] highlighted that the oscillating motion of the fluid is caused by the inner wall of the edge; that is, one side of the edge applies oscillating shear to the fluid, and the other side oscillates in its plane. Unlike the conventional nonslip boundary condition, this paper uses the second condition on shear stress to solve the oscillating motion of second-order fluid under mixed boundary conditions. The solution is expressed in the form of simple and multiple integrations under certain initial conditions to examine the effect of different Reynolds numbers (Re) on the fluid velocity. The rapid decompression system of the low-pressure chamber blasted under absolute seal is like a closed cylindrical pipe. Kondratov et al. [31] carried out oscillation analysis for a circular-section cylindrical elastic pipe, described it with the Kirchhoff–Love hypothesis, and deduced and solved it under the corresponding boundary conditions of the pressure harmonic change at the inlet and outlet of the pipe. They obtained the amplitude, phase frequency characteristics, and resonance frequency of the shell with high accuracy. However, this research method is applicable to the analysis of laminar flow with constant cross-sections. Some limitations and inaccuracies appear in the solution of an oscillating flow field with variable cross-sections.

Shivamoggi [32] highlighted that a dynamic impulse would be generated in the flow of compressible fluid. Kondratov et al. [31] deduced the expression of the hydrodynamic impulse in compressible fluid, established an appropriate impulse formula for the Euler equation, and determined the significance of applying this formula to compressible vortex rings. However, the actual application of the Benjamin variational characteristics of the moving axisymmetric vortex system has certain limitations. Through comparison, the stability of this structure appears questionable, and matching the theoretical results with the actual fluid flow seems challenging.

The fluid motion mode in the fast decompression system of the high-altitude chamber is the unsteady transient flow, and the vibration induced by the unsteady flow of the fluid is quite prevalent in many fields. Urbanowicz et al. [14] investigated the unsteady transient flow in a plastic pipe and used a simplified delayed strain solution to simulate the viscoelastic effect of the pipe wall during the transient flow process. The material properties and resonance frequency of the pipe will influence the transient pipe flow oscillation. Furthermore, [33] suggested a parametric polynomial approach for numerical analysis of the fluid-generated vibration of power equipment to examine complicated nonlinear systems. The researchers developed a set of numerical algorithms for

analyzing and solving the oscillating flow field. The altitude chamber, which is the focus of this study, is quite comparable with the parametric polynomial approach of the numerical analysis. Particularly, the parametric polynomial approach is employed in this study to investigate the fluid oscillation generated by fast decompression blasting.

In this study, polynomial parameters are used to simulate the rapid decompression of the altitude chamber, and the oscillation flow field is generated during the blasting process. The numerical analysis method is used to establish the pressure and velocity distribution equation of the oscillation flow field in the chamber under the condition of small incoming flow of the rapid decompression system. The decompression system can more accurately express the oscillation characteristics of the rapid decompression of the altitude chamber and has a certain role in preventing engineering accidents and reasonably using the altitude chamber for experiments.

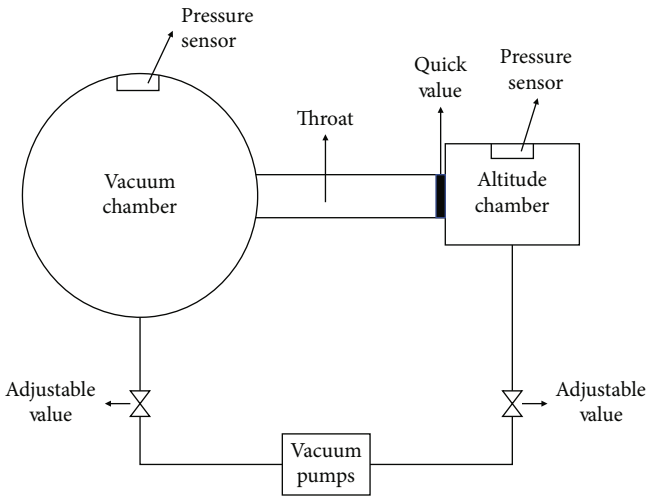

Figure 1: Rapid decompression system of the altitude chamber.

2. Physical Model

The rapid decompression system of the altitude chamber comprises a blasting chamber, a negative pressure source (negative pressure gas storage chamber), a pipeline, and an explosion rapid decompression mechanism. The quick valve device is opened using the pressure difference between the laboratory and vacuum chamber and the lever principle, and the blasting decompression time is 100–250 ms [4]. To meet the technical conditions and save costs, the chamber capacity ratio of the blasting and negative pressure chambers should be greater than 1 : 50 [34].

Figure 1 shows a plan view of the rapid decompression system of the altitude chamber. The vacuum system is mainly a negative pressure source for extracting vacuum. A single vacuum pump cannot achieve 100–300 ms of rapid vacuum pumping for the explosion chamber. Therefore, the vacuum system is used to store the vacuum of the vacuum chamber and connect it to the altitude chamber to achieve rapid vacuum pumping [35].

Figure 2 depicts the effective simplified model of the rapid decompression system and rapid decompression mechanism. Figure 2(a) includes two chambers; Figure 2(a), 1 is the negative pressure source (negative pressure storage room); Figure 2(a), 2 is the quick decompression mechanism (Figures 2(b)–2(d)); Figure 2(a), 3 is the throat pipe; and Figure 2(a), 4 is the altitude chamber. The cylinder powers the quick mechanism, and the pressure difference between the two compartments is used to achieve the rapid decompression. The throat tube is directly connected to the negative pressure chamber, and the rapid decompression mechanism controls the connection condition between the two chambers.

The quick pressure-reducing mechanism is located at the end face of the connecting pipe, which is opened and closed by the air cylinder. The advantage of this technique is that an open door is always in the shape of a bell mouth, with a large flow area, low resistance to airflow, and an increased gas flow rate. When the door is opened 14°, there is enough gas flow area. However, without fully opening, the air pressure can be quickly balanced. Particularly, the combined effect of the door's weight, the pressure difference between the decompression and negative pressure chambers, and the cylinder's thrust can be used to increase the valve's opening time, allowing it to open quickly and thus shortening the balancing time.

The quick decompression mechanism works by filling the air tank with 0.8–1.2 MPa air prior to the rapid decompression. When the rapid decompression is performed, the solenoid valve behind the air tank immediately opens. The high-pressure gas enters the cylinder through the high-pressure hose, and hence, the cylinder accelerates rapidly. The push plate at the front of the cylinder pushes the lock, causing the blasting mechanism's hatch to open quickly and achieve the rapid balance of the air pressure height on both sides of the hatch.

The following is the working principle of the rapid decompression system of the altitude chamber: before decompression, the quick valve mechanism is closed; the vacuum pump pumps the negative pressure chamber to low pressure with a very low absolute pressure and the blasting chamber to low pressure with a relatively high absolute pressure. On the premise of a relative pressure difference, when quick valve 2 will quickly open, the gas pressure will immediately flow from the higher blasting chamber to the lower negative pressure chamber, and the pressure difference between the two chambers will rapidly decrease. The pressure of the two chambers finally reaches equilibrium, and the decompression time can reach 100 ms.

3. Mathematical Model

Fluid-induced excitation is always a major problem in fluid-related engineering. In the fluid flow process, complex flow fields are often formed, and complex flow fields are difficult to theoretically study [15, 16, 36]. When examining the fluid excitation problem in power machinery, researchers have established a set of numerical methods for analyzing and solving the oscillating flow field (the parametric polynomial method). For the fluid oscillation generated by the rapid decompression system in the middle and altitude chambers,

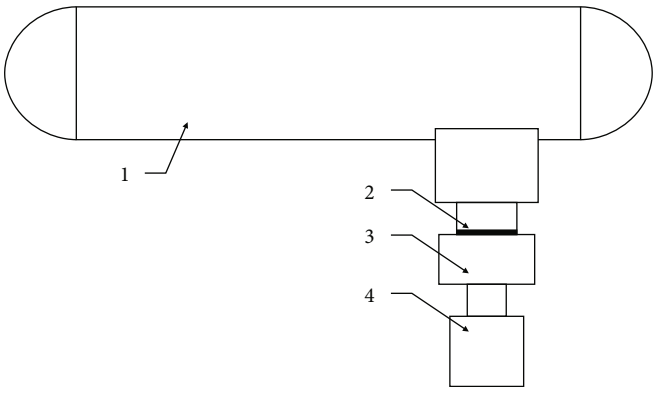

(a)

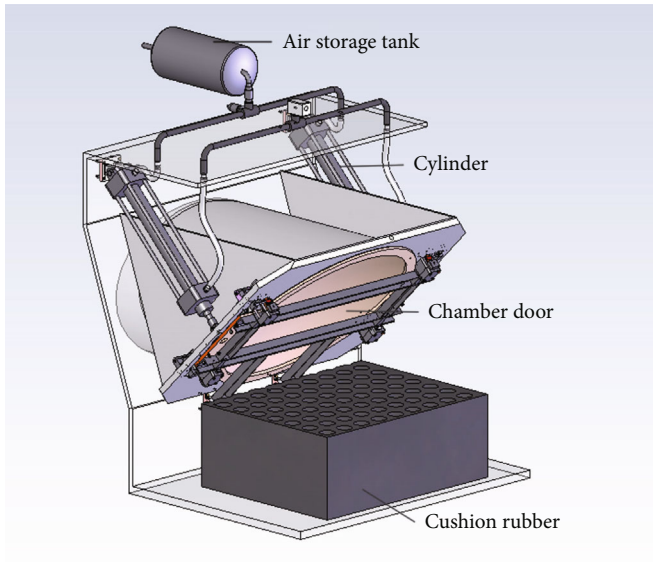

(b)

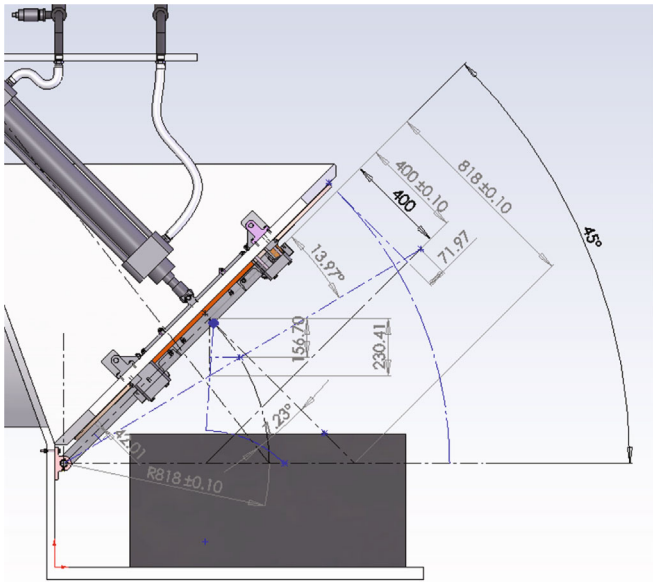

(c)

(d)

Figure 2: Quick decompression mechanism.

this method is applied to this project for the first time, and the numerical solution of the flow field is obtained through theoretical analysis.

Zuoyi et al. [13] suggested that any oscillatory flow is essentially a nonconstant flow; nonconstant flow parameters q (velocity, pressure, and density) are a function of spatial and temporal coordinates. Further, under microamplitude oscillation conditions, any nonconstant flow parameter $q(x, y, z, t)$ can be regarded as a linear superposition of the constant quantity $\tilde{q}(x, y, z, t)$ and the oscillatory quantity $\hat{q}(x, y, z, t)$ under microamplitude oscillation conditions. That is,

$$q(x, y, z, t) = \tilde{q}(x, y, z, t) + \hat{q}(x, y, z, t). \quad (1)$$

Therefore, the oscillating flow field under the conditions of microamplitude simple harmonic oscillations is required as the basic starting point in the study of the oscillatory fluid dynamics.

3.1. Analysis of the Oscillating Flow Field in the Tube. The flow form examined in this study is the variable section pipe flow (Figure 3).

Pipe portion A is a fixed-section pipe; part $A - B$ is an enlarged pipe, and the entire part $A - C$ is a decreased pipe. The flow field according to oscillatory hydrodynamics is a compressible viscous constant flow field. Assuming that the pipe diameter is R, the R change rule with axial Z may be written as follows:

$$R(z) = \Delta R + \frac{\Delta k}{2}\left(1 + \cos\frac{\pi z}{z_0}\right). \quad (2)$$

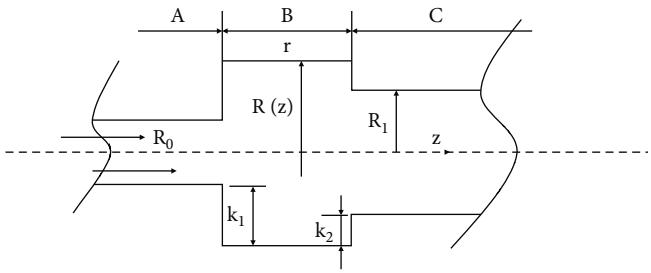

Figure 3: Schematic diagram of the variable section pipeline.

For the rapid decompression process, the following physical characteristics are considered according to the actual fluid flow:

(1) Flow axis symmetry

(2) Flow without tangential velocity

(3) No pressure change along the r direction

(4) Neglecting the second-order partial derivatives along the mainstream direction

(5) Two-dimensional viscous constant flow

Considering physical characteristics (1)-(5), the basic equations of the constant flow in the cylindrical coordinate system are as follows:

Continuous equations:

$$\frac{\partial(\rho r V_r)}{\partial r} + \frac{\partial(\rho V_z)}{\partial z} = 0. \tag{3}$$

N-S equation:

$$\begin{cases} V_r \dfrac{\partial V_z}{\partial r} + V_z \dfrac{\partial V_z}{\partial z} = -\dfrac{1}{\rho}\dfrac{\partial P}{\partial z} + \upsilon\left(\dfrac{\partial^2 V_z}{\partial r^2} + \dfrac{1}{r}\dfrac{\partial V_z}{\partial r} + \dfrac{\partial^2 V_z}{\partial z^2}\right), \\ V \dfrac{\partial V_r}{\partial r} + V_z \dfrac{\partial V_r}{\partial z} = -\dfrac{1}{\rho}\dfrac{\partial P}{\partial r} + \upsilon\left(\dfrac{\partial^2 V_r}{\partial r^2} + \dfrac{1}{r}\dfrac{\partial V_r}{\partial r} + \dfrac{\partial^2 V_r}{\partial z^2} - \dfrac{V_r}{r^2}\right). \end{cases} \tag{4}$$

Basic Equations (3)–(4) are used as the fundamental equations to solve the oscillatory flow field. The following are the main solution objectives:

(1) Constant polynomial parametric model for the micro incoming flow of the steady flow field

(2) Constant polynomial parametric model for micro incoming flow of the oscillatory flow field

3.1.1. Stable Flow Field for Tiny Incoming Flow. The new control equations can be obtained from the control equations in the cylindrical coordinate system and the constraints in Section 3.1.

Continuous equations:

$$\frac{\partial \tilde{V}z}{\partial z} + \frac{\partial \tilde{V}r}{\partial r} + \frac{\tilde{V}r}{r} = 0. \tag{5}$$

N-S equation:

$$\begin{cases} \tilde{V}r \dfrac{\partial \tilde{V}z}{\partial r} + \tilde{V}x \dfrac{\partial \tilde{V}z}{\partial z} = -\dfrac{1}{\rho}\dfrac{\partial \widetilde{\widehat{P}}}{\partial z} + \upsilon\left(\dfrac{\partial^2 \tilde{V}z}{\partial r^2} + \dfrac{1}{r}\dfrac{\partial \tilde{V}z}{\partial r} + \dfrac{\partial^2 \tilde{V}z}{\partial z^2}\right), \\ \tilde{V}r \dfrac{\partial \tilde{V}r}{\partial r} + \tilde{V}z \dfrac{\partial \tilde{V}r}{\partial z} = -\dfrac{1}{\rho}\dfrac{\partial \widetilde{\widehat{P}}}{\partial r} + \upsilon\left(\dfrac{\partial^2 \tilde{V}r}{\partial r^2} + \dfrac{1}{r}\dfrac{\partial \tilde{V}r}{\partial r} + \dfrac{\partial^2 \tilde{V}r}{\partial z^2} - \dfrac{\tilde{V}r}{r^2}\right). \end{cases} \tag{6}$$

The pressure in Equation (6) is represented by $\widehat{P}$. To distinguish the following dimensionless quantities, $\tilde{V}z$ and $\tilde{V}r$ are axial and radial flow rates, respectively, and υ is the fluid kinematic viscosity coefficient. However, in practical considerations, the internal fluid is dominated by the axial flow rate, and its radial flow rate is negligible. Therefore, Equation (6) can be expressed as

$$\begin{cases} \tilde{V}r \dfrac{\partial \tilde{V}z}{\partial r} + \tilde{V}z \dfrac{\partial \tilde{V}z}{\partial z} = -\dfrac{1}{\rho}\dfrac{\partial \widetilde{\widehat{P}}}{\partial z} + \nu\left(\dfrac{\partial^2 \tilde{V}z}{\partial r^2} + \dfrac{1}{r}\dfrac{\partial \tilde{V}z}{\partial r}\right), \\ \dfrac{\partial \tilde{P}}{\partial r} = 0. \end{cases} \tag{7}$$

For calculation simplicity, the following equation is dimensionless:

$$\begin{aligned} y &= \frac{r}{R_0}, \\ x &= \frac{z}{R_0}, \\ \omega &= \frac{Vz}{U_o}, \\ \upsilon &= \frac{Vr}{U_o}, \\ P &= \frac{\widehat{p}}{\rho U^2{}_o}, \\ \mathrm{Re} &= \frac{2R_0 U}{\nu}, \\ R &= \frac{R'}{R_0}. \end{aligned} \tag{8}$$

Here, R_0 is the radius of the pipe section, U_o is the average flow rate of pipe flow, Re is the Reynolds number, and R' is the radius of the pipe wall.

Therefore, the dimensionless equation is obtained as

$$\begin{cases} \dfrac{\partial \tilde{\omega}}{\partial x} + \dfrac{\partial \tilde{v}}{\partial y} + \dfrac{\tilde{v}}{y} = 0, \\ \tilde{\omega}\dfrac{\partial \tilde{\omega}}{\partial x} + \tilde{v}\dfrac{\partial \tilde{\omega}}{\partial y} = -\dfrac{\partial \tilde{P}}{\partial x} + \dfrac{2}{\mathrm{Re}}\left(\dfrac{\partial^2 \tilde{\omega}}{\partial y^2} + \dfrac{1}{y}\dfrac{\partial \tilde{\omega}}{\partial y}\right). \end{cases} \tag{9}$$

Variable substitution is performed as

$$\begin{aligned} \eta &= y^2, \\ u &= 2yv. \end{aligned} \tag{10}$$

Therefore, Equation (9) is converted to

$$\begin{cases} \dfrac{\partial \tilde{\omega}}{\partial x} + \dfrac{\partial \tilde{u}}{\partial \eta} = 0, \\ \tilde{\omega}\dfrac{\partial \tilde{\omega}}{\partial x} + \tilde{u}\dfrac{\partial \tilde{\omega}}{\partial \eta} = -\dfrac{\partial \tilde{P}}{\partial x} + \dfrac{8}{\mathrm{Re}}\dfrac{\partial}{\partial \eta}\left(\eta\dfrac{\partial \tilde{\omega}}{\partial \eta}\right). \end{cases} \tag{11}$$

Boundary conditions:

$$\begin{cases} \eta = R^2 \longrightarrow \tilde{\omega} = 0, \quad \tilde{u} = 0, \\ \eta = 0 \longrightarrow \tilde{u} = 0, \quad \dfrac{\partial \tilde{\omega}}{\partial y} = 0. \end{cases} \tag{12}$$

The flow in the chamber may return at the variable section; thus, the third-degree polynomial of η is used.

$$\tilde{\omega} = R^{-2}\left(R^2 - \eta\right)\left[a_1(x) + a_2(x)\eta + a_3(x)\eta^2\right]. \tag{13}$$

Here, $a_1(x)$, $a_2(x)$, and $a_3(x)$ are polynomial coefficients, which are functions containing coordinate x. To make the equation more solvable, the integral solution is used. The flow integral equation is expressed as

$$\frac{d}{dx}\int_0^{R^2} \tilde{\omega}\, d\eta = 0. \tag{14}$$

Multiplying Equation (11) (continuity equation) with its momentum equation and adding and integrating to obtain the momentum integral equation,

$$\frac{d}{dx}\int_0^{R^2} \tilde{\omega}^2 d\eta = -R^2\frac{d\tilde{P}}{dx} + \frac{8}{\mathrm{Re}}\left(\eta\frac{\partial \tilde{\omega}}{\partial \eta}\right)_{\eta=R^2}. \tag{15}$$

Multiplying Equation (11) by 2ω and momentum equation times ω^2, the momentum integral equation is obtained by summing and integrating the following:

$$\frac{d}{dx}\int_0^{R^2} \tilde{\omega}^3 d\eta = -2\frac{d\tilde{P}}{dx} - \frac{16}{\mathrm{Re}}\int_0^{R^2} \eta\left(\frac{\partial \tilde{\omega}}{\partial \eta}\right)^2 d\eta. \tag{16}$$

Since the pressure parameter P is constant along the cross section, $P = a_4(x)$, and four equations are required to solve coefficients $a_1(x)$, $a_2(x)$, $a_3(x)$, and $a_4(x)$. Thus, the momentum equation is established at $\eta = 0$.

$$\left[\tilde{\omega}\frac{\partial \tilde{\omega}}{\partial x}\right]_{\eta=0} = -\frac{\partial \tilde{P}}{\partial x} + \frac{8}{\mathrm{Re}}\left[\frac{\partial}{\partial \eta}\left(\eta\frac{\partial \tilde{\omega}}{\partial \eta}\right)\right]_{\eta=0}. \tag{17}$$

At this point, all these coefficients are functions containing only x. Thus, all the partial derivatives of the coefficients can be written as full derivatives. The parametric polynomial of ω yields $\partial\tilde{\omega}/\partial\eta$.

$$\frac{\partial \tilde{\omega}}{\partial \eta} = \left(a_2 - R^{-2}a_1\right) + 2\left(a_3 - R^{-2}a_2\right)\eta - 3R^{-2}a_3\eta^2. \tag{18}$$

Using Equations (13) and (18) solves Equations (14)–(17), respectively:

$$\begin{cases} \dfrac{da_1}{dx} + \zeta_1\dfrac{da_2}{dx} + \zeta_2\dfrac{da_3}{dx} = \zeta_3, \\ \vartheta_1\dfrac{da_1}{dx} + \vartheta_2\dfrac{da_2}{dx} + \vartheta_3\dfrac{da_3}{dx} + \dfrac{da_4}{dx} = \vartheta_4, \\ \varpi_1\dfrac{da_1}{dx} + \varpi_2\dfrac{da_2}{dx} + \varpi_3\dfrac{da_3}{dx} + \dfrac{da_4}{dx} = \varpi_4, \\ \lambda_1\dfrac{da_1}{dx} + \dfrac{da_4}{dx} = \lambda_2. \end{cases} \tag{19}$$

In Equation (19),

$$\zeta_1 = \frac{1}{3}R^2,$$

$$\zeta_2 = \frac{1}{6}R^4,$$

$$\zeta_3 = -\left(\frac{2a_1}{R} + \frac{4}{3}R + R^3\right)\frac{dR}{dx},$$

$$\vartheta_1 = \frac{2}{3}a_1 + \frac{1}{6}R^2a_2 + \frac{1}{15}R^4a_3,$$

$$\vartheta_2 = \frac{1}{6}R^2a_1 + \frac{1}{15}R^4a_2 + R^3a_3,$$

$$\vartheta_3 = \frac{1}{15}R^4a_1 + \frac{1}{30}R^6a_2 + \frac{2}{105}R^8a_3,$$

$$\vartheta_4 = -\frac{8}{\mathrm{Re}}\frac{1}{R^2}\left(a_1 + R^2a_2 + R^4a_3\right) - \left(\frac{2}{3}\frac{{a_1}^2}{R} + \frac{1}{5}R^3{a_2}^2 + \frac{2}{21}R^7{a_3}^2 + \frac{2}{3}Ra_1a_2 + \frac{3}{5}R^3a_1a_3 + \frac{4}{15}R^5a_2a_3\right)\frac{dR}{dx}.$$

$$\varpi_1 = \frac{R^2}{2}\left(\frac{3}{4}{a_1}^2 + \frac{3}{10}R^2a_1a_2 + \frac{1}{20}R^4{a_2}^2 + \frac{1}{10}R^4a_1a_3 + \frac{3}{70}R^6a_2a_3 + \frac{3}{280}R^8{a_3}^2\right),$$

$$\varpi_2 = \frac{R^4}{2}\left(\frac{3}{20}{a_1}^2 + \frac{1}{10}R^2a_1a_2 + \frac{3}{140}R^4{a_2}^2 + \frac{3}{70}R^4a_1a_3 + \frac{3}{140}R^6a_2a_3 + \frac{1}{168}R^8{a_3}^2\right),$$

$$\varpi_3 = \frac{R^6}{2}\left(\frac{1}{20}{a_1}^2 + \frac{3}{70}R^2a_1a_2 + \frac{3}{280}R^4{a_2}^2 + \frac{3}{140}R^4a_1a_3 + \frac{1}{84}R^6a_2a_3 + \frac{1}{280}R^8{a_3}^2\right),$$

$$\varpi_4 = -\frac{8}{\mathrm{Re}}\left(\frac{1}{2}{a_1}^2 + \frac{1}{6}R^4{a_2}^2 + \frac{1}{10}R^8{a_3}^2 + \frac{1}{3}R^2a_1a_2 + \frac{7}{30}R^6a_2a_3 + \frac{1}{6}R^4a_1a_3\right) - \frac{R}{2}\left(\frac{1}{2}{a_1}^3 + \frac{2}{35}R^6{a_2}^3 + \frac{1}{60}R^{12}{a_3}^2 + \frac{3}{5}R^2{a_1}^2a_2 + \frac{3}{10}R^4a_1{a_2}^2 + \frac{3}{10}R^4{a_1}^2a_3 + \frac{12}{35}R^6a_1a_2a_3 + \frac{3}{28}R^8a_1{a_2}^2 + \frac{3}{28}R^8a_2{a_3}^2 + \frac{1}{14}R^{10}a_2{a_3}^2\right)\frac{dR}{dx},$$

$$\lambda_1 = a_1,$$

$$\lambda_2 = -\frac{8}{\mathrm{Re}}\left(\frac{a_1}{R^2} - a_2\right). \tag{20}$$

Equation (19) has four pending values: da_1/dx, da_2/dx, da_3/dx, and da_4/dx. All other parameters contain only the coordinates of a_1, a_2, a_3, a_4, and R. The velocity distribution on the initial cross-section is known. Hence, the unknown parameters can be found, and the association yields

$$\frac{da_3}{dx} = \frac{\{[\vartheta_2 - \zeta_1(\vartheta_1 - \lambda_1)][\varpi_4 - \lambda_2 - \zeta_3(\varpi_1 - \lambda_1)] - [\vartheta_4 - \lambda_2 - \zeta_3(\vartheta_1 - \lambda_1)][\varpi_2 - \zeta_1(\varpi_1 - \lambda_1)]\}}{\{[\vartheta_2 - \zeta_1(\vartheta_1 - \lambda_1)][\varpi_3 - \zeta_2(\varpi_1 - \lambda_1)] - [\vartheta_3 - \zeta_2(\vartheta_1 - \lambda_1)][\varpi_2 - \zeta_1(\varpi_1 - \lambda_1)]\}}, \tag{21}$$

$$\frac{da_2}{dx} = \frac{\{[\vartheta_3 - \zeta_2(\vartheta_1 - \lambda_1)][\varpi_4 - \lambda_2 - \zeta_3(\varpi_1 - \lambda_1)] - [\vartheta_4 - \lambda_2 - \zeta_3(\vartheta_1 - \lambda_1)][\varpi_3 - \zeta_2(\varpi_1 - \lambda_1)]\}}{\{[\vartheta_3 - \zeta_2(\vartheta_1 - \lambda_1)][\varpi_2 - \zeta_1(\varpi_1 - \lambda_1)] - [\zeta_1(\vartheta_1 - \lambda_1)][\varpi_3 - \zeta_2(\varpi_1 - \lambda_1)]\}}, \tag{22}$$

$$\frac{da_1}{dx} = \zeta_3 - \zeta_1\frac{da_2}{dx} - \zeta_2\frac{da_3}{dx}, \tag{23}$$

$$\frac{da_4}{dx} = \lambda_2 - \lambda_1\frac{da_1}{dx}. \tag{24}$$

The derivatives of the four coefficients can be obtained using Equations (21)–(24). Then, we can obtain a_1–a_4 and the full field of ω and P.

$$\tilde{u} = \frac{\left\{-\tilde{\omega}\left[\left(1 - \left(\eta/R^2\right)\right)\left((da_1/dx) + \left((da_2/dx)\eta\right) + \left((da_3/dx)\eta^2\right)\right) + \left(\left(2\eta\left(a_1 + a_2\eta + a_3\eta^2\right)\right)(dR/dx)/R^3\right)\right] - \left(d\tilde{P}/dx\right) + (8/\mathrm{Re})\left[\left(a_2 - R^{-2}a_1\right) + 4\left(a_3 - R^{-2}a_2\right)\right]\right\}}{\left[\left(a_2 - R^{-2}a_1\right) + 2\left(a_3 - R^{-2}a_2\right)\eta - 3R^{-2}a_3\eta^2\right]}. \tag{25}$$

The small incoming flow field distribution of the variable cross-section pipe is solved by using the parametric polynomial method. The fourth-order Runge–Kutta methods are used for the iterative solution under the initial conditions of different flow parameters. Unless otherwise specified, the calculation results are dimensionless.

The throat diameter is uniform in the flow field model generated by microflow. Figure 4 depicts the velocity and pressure distributions of the throat.

Figure 4(a) depicts the distribution of velocity amplitudes in a constant cross-section tube at various Re. The degree of velocity oscillation increases as Re increases, and the negative gradient velocity appears, representing the negative direction velocity of negative pressure.

Figure 4(b) depicts the pressure amplitude distribution in a constant cross-section tube at various Re. As Re increases, a small pressure oscillation phenomenon appears, where the negative gradient pressure represents the negative pressure change in the negative direction.

Figure 5(a) depicts the distribution of velocity amplitudes in a pipe with a steadily expanding cross section. The airflow movement in the altered cross-section becomes

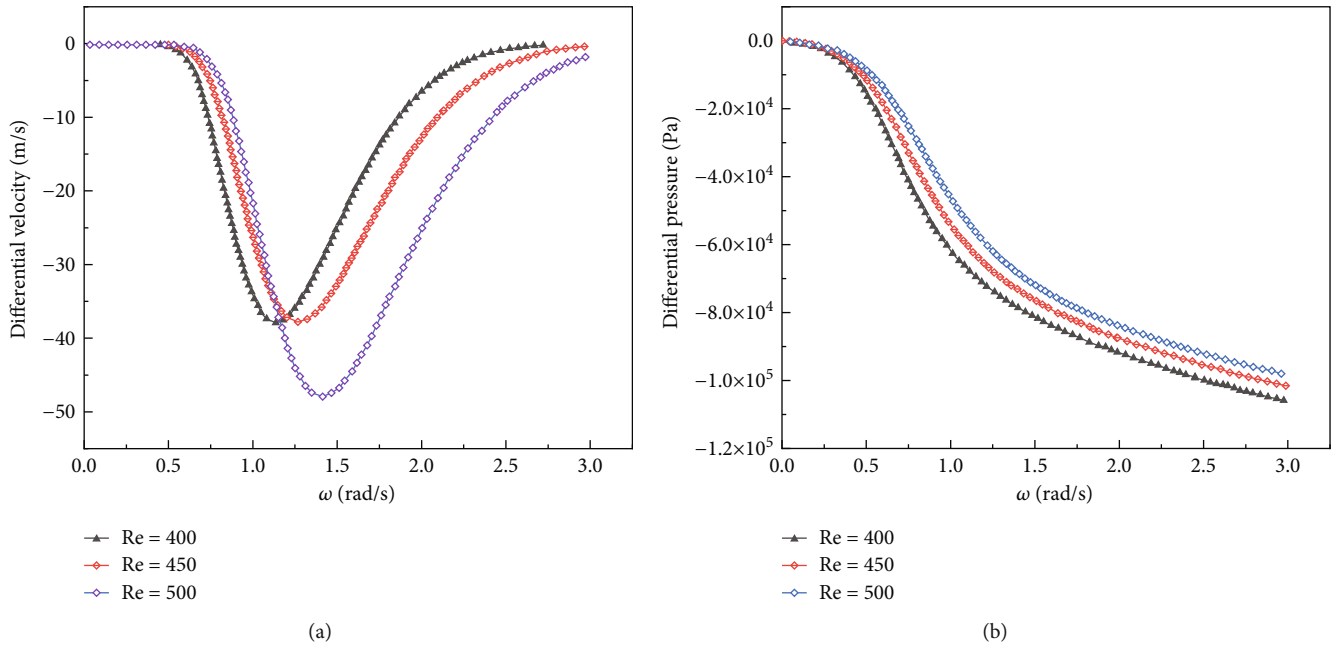

Figure 4: Distribution of the steady flow field in the constant cross-section pipe at a certain time.

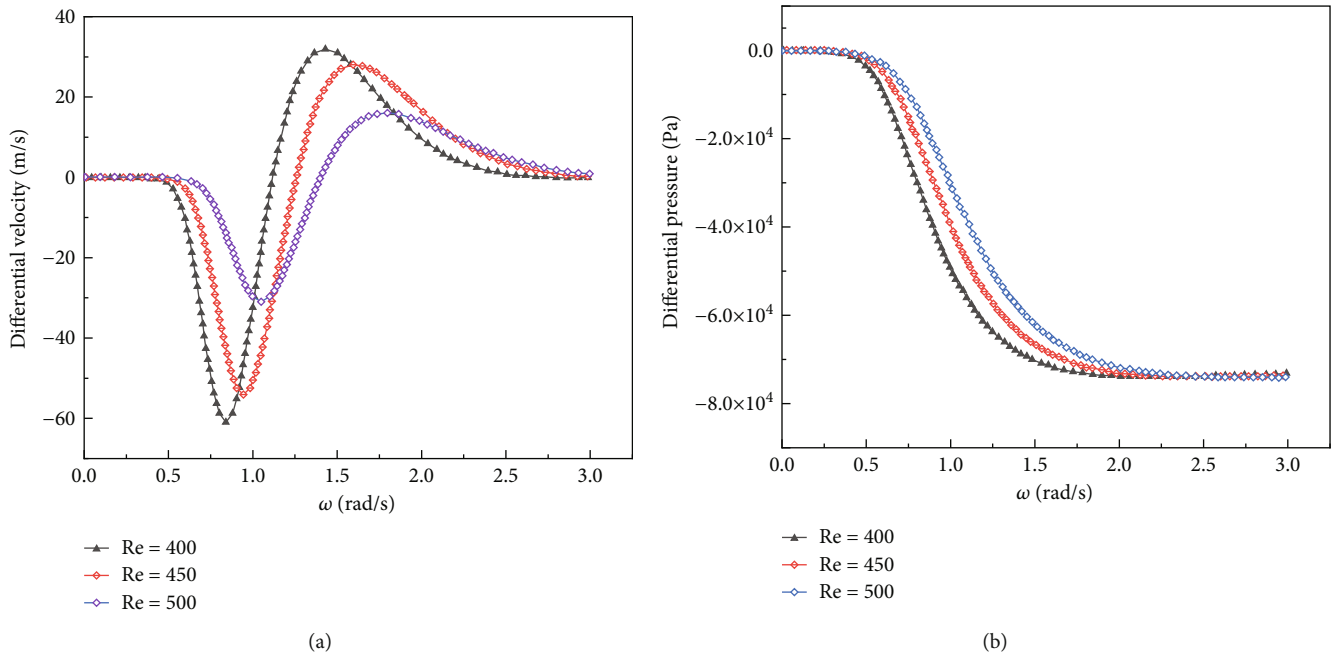

Figure 5: Distribution of the steady flow field in an expanding pipe at a given time.

unstable. Slower speed and quicker changing speed result from increasing Re. Velocity backflow occurs in a relatively short time.

Figure 5(b) depicts the pressure amplitude distribution in a pipe with progressively increased cross-section. The pressure in the pipe with the variable cross-section reaches its highest point quickly and gradually balances. Further, the reaction to the pressure oscillation phenomena grows faster as Re increases.

The following are the iteration results:

(1) There is no evident backflow in the steady flow field of the constant cross-section pipe

(2) There is visible backflow in the steady flow field in the variable cross-section pipe

(3) The flow velocity in the throat passage of a variable cross-section pipe will drop, but backflow will still occur and become more problematic in the same cross-section pipe. This is also connected to the

cross-sectional size of the pipe; therefore, flow in different diameters of pipes will vary

This paper only examines the flow in pipes with a uniform cross-section. The negative pressure gradient shown in Figures 4 and 5 is the relative pressure change. Reflux occurs in the central area of the pipe and flows back and forth between the central and wall areas, and the speed will gradually decrease. Even in such a small incoming flow model, turbulence can occur repeatedly.

3.1.2. Oscillating Flow Field of Micro Incoming Flow. The following results can be obtained using the same analysis method as the steady flow field:

Continuous equations:

$$\frac{\partial \omega}{\partial x} + \frac{\partial u}{\partial \eta} = 0. \tag{26}$$

Momentum equation:

$$\omega \frac{\partial \omega}{\partial x} + \tilde{u} \frac{\partial \omega}{\partial \eta} + \frac{R'}{u_0} \frac{\partial \omega}{\partial t} = -\frac{\partial P}{\partial x} + \frac{8}{\mathrm{Re}} \frac{\partial}{\partial \eta} \left(\eta \frac{\partial \omega}{\partial \eta} \right). \tag{27}$$

A derivative of velocity exists with respect to time in the oscillating flow field; hence, there is more R'/u_0 and $\partial\omega/\partial t$ here than that in the steady field.

In oscillatory hydrodynamics, the basic relationship for velocity is $\omega = \tilde{\omega} + \bar{\omega} e^{i\omega t}$ and $u = \tilde{u} + \bar{u} e^{i\omega t}$. Substituting into Equations (26) and (27) yields

$$\frac{\partial \bar{\omega}}{\partial x} + \frac{\partial \bar{u}}{\partial \eta} = 0,$$

$$i\omega' \bar{\omega} + \tilde{u} \frac{\partial \bar{\omega}}{\partial \eta} + \tilde{\omega} \frac{\partial \bar{\omega}}{\partial x} + \bar{u} \frac{\partial \tilde{\omega}}{\partial \eta} + \bar{\omega} \frac{\partial \tilde{\omega}}{\partial x} = -\frac{\partial \bar{P}}{\partial x} + \frac{8}{\mathrm{Re}} \frac{\partial}{\partial \eta} \left(\eta \frac{\partial \bar{\omega}}{\partial \eta} \right). \tag{28}$$

In equation $\omega' = (R'/\tilde{u})\,\omega$, the axial flow rate amplitude is

$$\bar{\omega} = c_0(x)\left(R^2 - \eta\right)\left(c_1(x) - \eta\right). \tag{29}$$

Similarly, $c_0(x)$ and $c_1(x)$ in the equation are still polynomial coefficients, both as a function of coordinate x. To eliminate the unknown quantity $\bar{u}$ in Equations (26) and (27), by summing up the integrals in Equations (26) and (27), by summing up the integrals from R^2 by punching equations:

$$\begin{aligned} &\int_0^{R^2} i\omega' \bar{\omega} d\eta + 2\int_0^{R^2} \tilde{\omega} \frac{\partial \tilde{\omega}}{\partial x} d\eta + \int_0^{R^2} \bar{\omega} \frac{\partial \tilde{\omega}}{\partial x} d\eta + \int_0^{R^2} \tilde{u} \frac{\partial \bar{\omega}}{\partial \eta} d\eta \\ &\quad = -\int_0^{R^2} \frac{\partial \bar{P}}{\partial x} d\eta + \int_0^{R^2} \frac{8}{\mathrm{Re}} \frac{\partial}{\partial \eta} \left(\eta \frac{\partial \bar{\omega}}{\partial \eta} \right) d\eta. \end{aligned} \tag{30}$$

Bringing $\bar{\omega}$ and $\tilde{\omega}$ into Equation (30) achieves

$$\psi_1 \frac{\partial c_0}{\partial x} + \psi_2 \frac{\partial c_1}{\partial x} = \kappa_1. \tag{31}$$

In Equation (31),

$$\begin{aligned} \psi_1 &= \frac{2}{3} a_1 c_1 R^4 - \frac{1}{6} a_1 R^6 + \frac{1}{6} a_2 c_1 R^6 - \frac{1}{15} a_2 R^8 \\ &\quad + \frac{1}{15} a_3 c_1 R^8 - \frac{1}{30} a_3 R^{10}, \\ \psi_2 &= \frac{2}{3} a_1 c_0 R^4 + \frac{1}{6} a_2 c_0 R^6 + \frac{1}{15} a_3 c_0 R^8, \\ \kappa_1 &= -\frac{16}{\mathrm{Re}} c_0 {R_b}^4 - \kappa_2 - \kappa_3 - \kappa_4 - \kappa_5 - \kappa_6, \\ \kappa_3 &= 2c_0 \left[\left(\frac{R_2}{R_1} - 1 \right) \frac{R_1}{z_0} \right] \left[\frac{1}{2} a_1 c_1 R^3 - \frac{1}{6} a_1 R^5 + \frac{1}{6} a_2 c_1 R^5 \right. \\ &\quad \left. - \frac{1}{12} a_2 R^7 + \frac{1}{12} a_3 c_1 R^7 - \frac{1}{20} a_3 R^9 \right], \\ \kappa_4 &= c_0 \left[\frac{1}{3} c_1 \frac{\partial a_1}{\partial x} R^4 - \frac{1}{12} \frac{\partial a_1}{\partial x} R^6 + \frac{1}{12} c_1 \frac{\partial a_2}{\partial x} R^6 - \frac{1}{30} \frac{da_2}{dx} R^8 \right. \\ &\quad \left. + \frac{1}{30} \frac{da_3}{dx} R^8 - \frac{1}{60} \frac{da_3}{dx} R^{10} \right], \\ \kappa_5 &= 2c_0 \left[\left(\frac{R_2}{R_1} - 1 \right) \frac{R_1}{z_0} \right] \left[\frac{1}{2} a_1 c_1 R - \frac{1}{6} R^3 a_1 + \frac{1}{6} a_2 c_1 R^3 \right. \\ &\quad \left. - \frac{1}{12} a_2 R^5 + \frac{1}{12} a_3 c_1 R^5 - \frac{1}{20} a_3 R^7 \right], \\ \kappa_6 &= \int_0^{R^2} \left\{ \frac{\partial a_4}{\partial x} + \frac{8}{\mathrm{Re}} \frac{1}{R^2} \left[\left(a_1 - a_2 R^2 \right) + 4\left(a_2 - a_3 R^2 \right) \eta + 9 a_3 \eta^2 \right] \right. \\ &\quad + \left(1 - \frac{\eta}{R^2} \right) \left(a_1 + a_2 \eta + a_3 \eta^2 \right) \left[\left(1 - \frac{\eta}{R^2} \right) \right. \\ &\quad \cdot \left(\frac{da_1}{dx} + \frac{da_2}{dx} \eta + \frac{da_3}{dx} \eta^2 \right) \\ &\quad \left. \left. + \frac{(2\eta(dR/dx))\left(a_1 + a_2 \eta + a_3 \eta^2 \right)}{R^3} \right] \right\} \\ &\quad \cdot \frac{\left[10\left(c_1 + R^2 - 2\eta \right) \right]}{\left[\left(a_2 R^2 - a_1 - 2a_2 \eta + 2a_3 R^2 \eta - 3a_3 \eta^2 \right) / R^2 \right]} d\eta, \end{aligned} \tag{32}$$

where all the coefficients are the functions of x. The partial derivative form is equivalent to the full derivative form. The boundary conditions at this point are expressed as

$$\begin{cases} \eta = 0 \longrightarrow \tilde{\omega} = a_1, \\ \bar{\omega} = c_0 c_1 R^2, \\ \tilde{u} = 0 \longrightarrow \bar{u} = 0, \end{cases} \tag{33}$$

$$\eta = 1 \longrightarrow \tilde{\omega} = 0, \bar{\omega} = 0, \tilde{u} = 0, \bar{u} = 0.$$

Substituting the boundary conditions into Equation (27)

yields

$$T_1 \frac{\partial c_0}{\partial x} + T_2 \frac{\partial c_1}{\partial x} = G_1, \tag{34}$$

$$\frac{\partial \bar{P}}{\partial x} = \frac{8}{\mathrm{Re}} \left[-c_0(1 + c_1) + 4c_0 R^2 \right]. \tag{35}$$

In Equation (35),
$T_1 = a_1 c_1 R^2$,
$T_2 = a_1 c_0 R^2$,

$$\begin{aligned} G_1 = &-\frac{32}{\mathrm{Re}} c_0 R^2 - i\omega' c_0 c_1 R^2 - \frac{da_1}{dx} c_0 c_1 R^2 \\ &- 2c_0 c_1 a_1 R^2 \left[\left(\frac{R_2}{R_1} - 1 \right) \frac{R_1}{z_0} \right] \\ &- \left(\frac{2c_0 c_1 a_1}{R} \right) \left[\left(\frac{R_2}{R_1} - 1 \right) \frac{R_1}{z_0} \right]. \end{aligned} \tag{36}$$

Similarly, Equations (29) and (30) can be solved as

$$\begin{aligned} \frac{dc_0}{dx} &= \frac{\kappa_1 T_2 - G_1 \psi_2}{\psi_1 T_2 - T_1 \psi_2}, \\ \frac{dc_1}{dx} &= \frac{\kappa_1 T_1 - G_1 \psi_1}{\psi_2 T_1 - T_2 \psi_1}. \end{aligned} \tag{37}$$

With the initial conditions dc_0/dx and dc_1/dx known, the fourth-order Runge - Kutta method is used iteratively to solve c_0 and c_1. The velocity amplitude $\bar{\omega}$ and pressure amplitude $\bar{P}$ are obtained for the entire flow field.

The oscillating flow field is iterated, and the results are as follows.

Figure 6(a) depicts the velocity amplitude distribution of a constant section pipe in an oscillating flow field. The velocity amplitude of the pipe exhibits a clear reflux reaction in a short period as Re increases, and an evident reflux state has already emerged in the low speed state in the negative direction.

Figure 6(b) depicts the pressure amplitude distribution in the oscillating flow field in the constant cross-section pipeline. The pressure in the pipeline becomes unstable as Re increases, and the pressure distribution in the negative direction exhibits visible oscillation.

Figure 7(a) depicts the velocity amplitude distribution in the oscillating flow field in the variable cross-section pipe. Multiple velocity backflows occur in a short period due to the airflow's unstable movement in the oscillating flow field. The fluid flow has turned turbulent at this point. This instability is the primary cause of the fluid flow oscillation and the resonance of the chamber's inner wall.

Figure 7(b) depicts the pressure amplitude distribution in the oscillating flow field in the variable cross-section pipe. The flow condition is exceedingly unstable turbulence at this moment, and the airflow movement is disorganized. There is visible pressure fluctuation in the variable cross-section pipe in a short time. Therefore, minor airflow movement will also have an effect on the chamber.

The iteration results indicate the following:

(1) In the flow of the fixed-section pipe, a slight backflow phenomenon occurs, and the flow velocity gradually decreases

(2) In the flow of the variable cross-section (expansion) pipe, backflow clearly occurs. Hence, the flow velocity will decrease, and the backflow phenomenon in the constant cross-section pipe will still occur and become more severe

(3) The pressure oscillation phenomenon in the oscillating flow field is evident, which is also related to the cross-sectional size of the pipe. The flow rate of different pipe sizes will vary. This study only examines the flow in a uniform cross-section pipe

In this section, the oscillatory flow field distribution of the micro inflow in the rapid decompression system is investigated by using oscillatory fluid dynamics. The differential equations of velocity distribution and pressure coefficient in the model are solved. The velocity and pressure parameters in the steady and oscillating flow fields under different conditions are obtained, and the oscillation characteristics in the throat pipe are analyzed.

4. Rapid Decompression Test

The two chambers are connected by an explosive rapid decompression mechanism, and the pressure difference between the low pressure and negative pressure chambers is used. The device is opened by the lever principle without requiring cylinder driving to realize the rapid explosive decompression. During the decompression process, the pressure transmitter is used to record the pressure change during the blasting process.

4.1. Introduction to Test Equipment. Equipment, including a vacuum system, pipeline valve, low-pressure chamber, negative pressure chamber, and explosion rapid decompression mechanism, mainly built the rapid decompression test of a low-pressure chamber.

4.1.1. Vacuum System and Test System. To meet the requirements of the extreme vacuum degree and height change rate of the low-pressure chamber and to ensure better efficiency and economy, the vacuum system is used to obtain the vacuum degree required for the test. The vacuum system is composed of a negative pressure chamber and a vacuum pump unit to meet the requirements of rapid decompression time and pressure, respectively.

The vacuum pump unit includes three German Leybold *sv300b* vacuum pumps and two *wau1001* roots vacuum pump units. The corresponding pipelines are adopted and reformed. The reformed vacuum pump unit meets the requirements of controllable pressure regulation of the test chamber and vacuum tank. As shown in Figure 1(c), a set of *sv300b* vacuum pump and *wau1001* roots pump can pump up to 730 m^3/h. The vacuum degree can reach $8 \times$

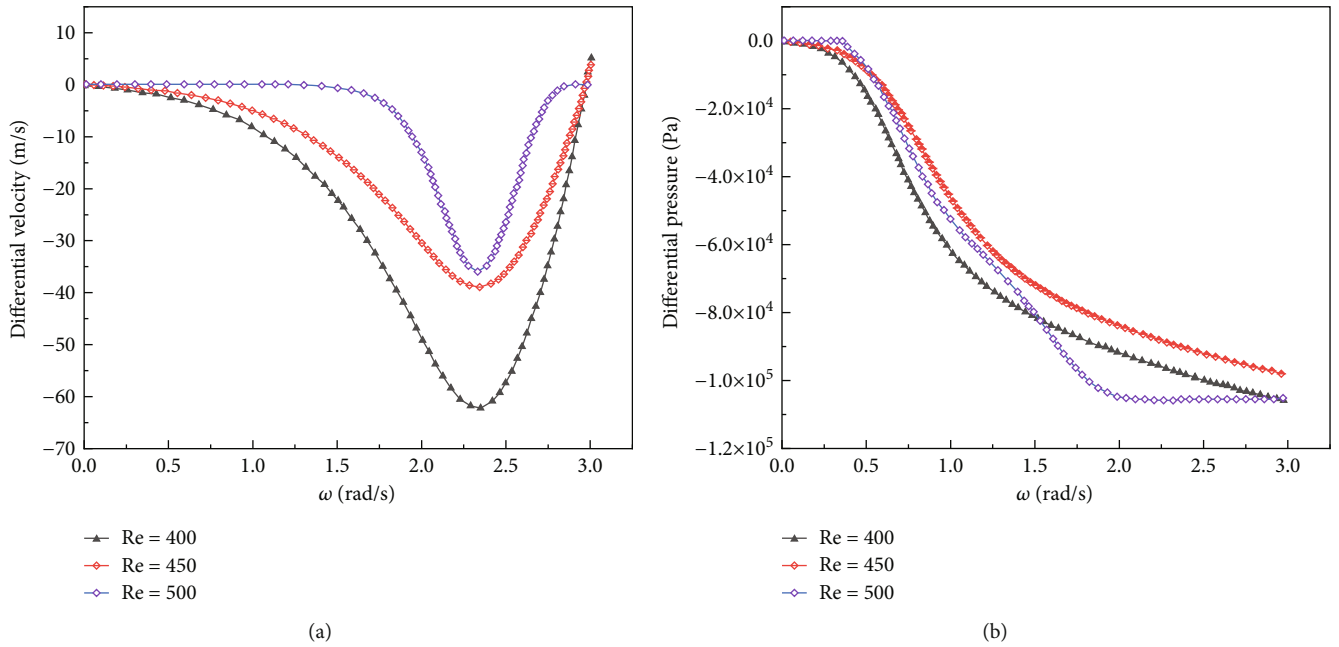

Figure 6: Distribution of the oscillating flow field in a fixed-section pipe at a certain time.

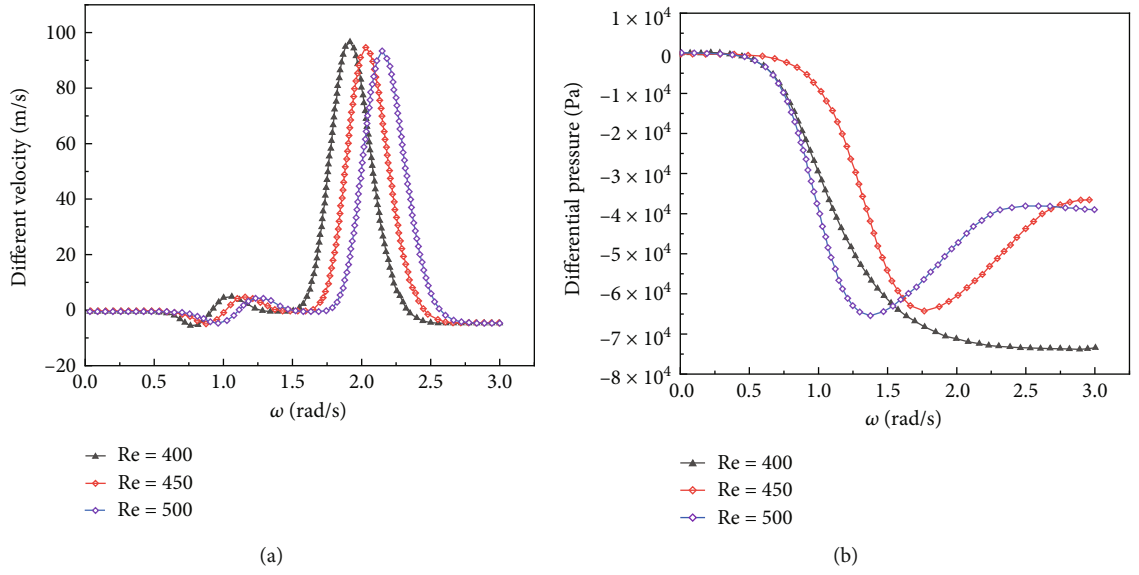

Figure 7: Distribution of the oscillating flow field in variable cross-section pipeline at a certain time.

10^{-3} m bar (higher than 30000 m), the two vacuum pumps work simultaneously, and the air extraction can reach 1.3/h. Therefore, the requirements of the working time of the vacuum chamber are met.

For the test system, the American NI-CDAQ-9178 chassis and NI-9208AI acquisition card are used to collect the pressure in the test chamber at a high speed. The upper computer software LabVIEW is used as the test system to obtain the real-time pressure change in the test chamber. Figure 8 shows the test system interface.

4.1.2. Altitude and Vacuum Chambers. The optimal ratio of the effective volume of the altitude chamber to the volume of the vacuum chamber, which is required to achieve the best test effect during the rapid decompression test, is more than 1 : 50 [26]. The effective volume of the altitude chamber is 2.59 m^3, and the volume of the vacuum chamber is 150 m^3. Figure 9 shows the test platform for the altitude and vacuum chambers.

The altitude and the vacuum chambers are connected using a rapid decompression mechanism, and the decompression time can reach 100–300 ms when the opening of the diameter port is 100% to realize the rapid decompression.

4.1.3. Other Types of Equipment. The pressure data acquisition mainly used in the rapid decompression system of the altitude chamber is the *HM-22* absolute pressure transmitter

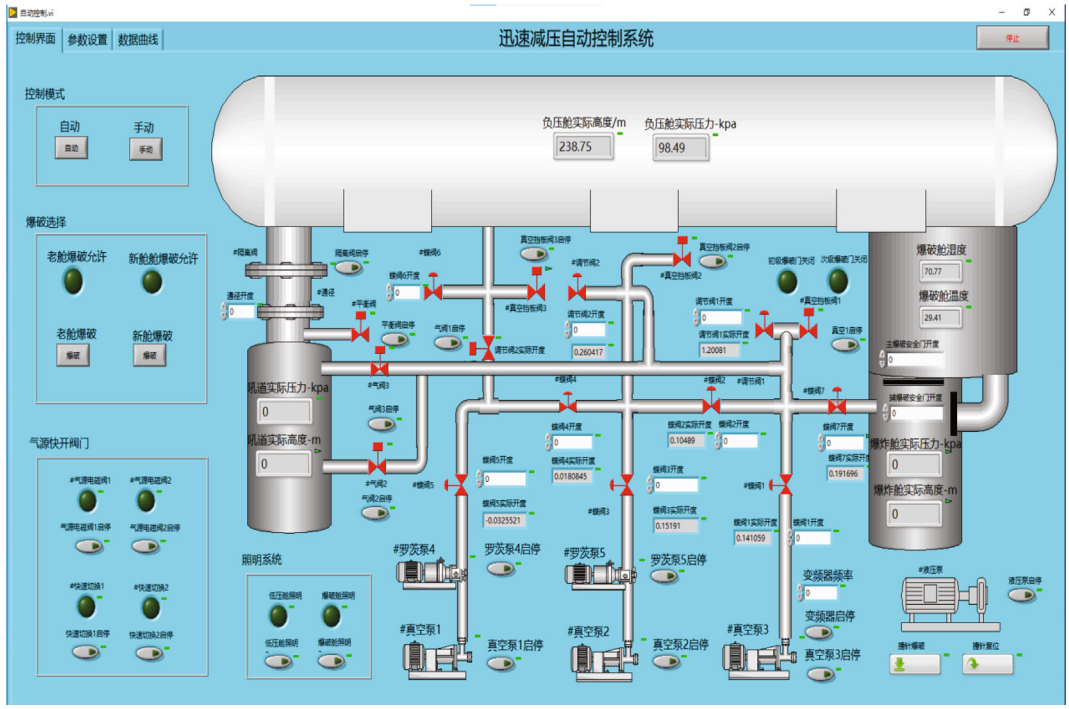

Figure 8: Rapid decompression test system.

(a) (b)

Figure 9: Altitude and vacuum chambers.

of *HELM AG*. The altitude and the vacuum chambers use the *HM-22* absolute pressure transmitter for real-time pressure detection. The high-precision transmitter can better analyze the pressure oscillation in the explosion test.

Valves are used to control the pipelines between the vacuum system and the altitude and vacuum chambers. These include adjustable butterfly, pneumatic, ball, and quick air breaking valves. The whole rapid decompression test system is composed of the main components.

4.2. Experimental Design. A rapid decompression test was designed for the altitude chamber to verify the oscillation characteristics during the test. The test process includes factors such as factor A (initial pressure of the negative pressure chamber), factor B (initial pressure of the altitude chamber), and factor C (pipe diameter). To obtain the exact optimal solution, the orthogonal experiment method is used to design the experiment. Due to equipment factors, the maximum differential pressure between the vacuum and altitude chambers is 60 kPa. Table 1 presents the orthogonal experimental design of this test.

Table 1: Orthogonal experimental design.

Test	Factor A	Factor B	Factor C	Differential pressure
①	15 kPa	75 kPa	800 mm	60 kPa
②	10 kPa	70 kPa	800 mm	60 kPa
③	5 kPa	65 kPa	800 mm	60 kPa
④	3.1 kPa	63.1 kPa	600 mm	60 kPa
⑤	7.56 kPa	45.20 kPa	600 mm	34.50 kPa
⑥	15 kPa	65 kPa	600 mm	50 kPa
⑦	15 kPa	70 kPa	500 mm	55 kPa
⑧	31 kPa	89 kPa	500 mm	58 kPa
⑨	17.5 kPa	58 kPa	500 mm	40.5 kPa

4.3. Analysis of the Experimental Results. The rapid decompression experiment was carried out according to the

Table 2: Orthogonal experimental design.

Test	Pipe diameter	Differential pressure	Equilibrium pressure	Decompression time	Maximum oscillation value
①	800 mm	60 kPa	16.17 kPa	121 ms	0.32 kPa
②	800 mm	60 kPa	11.18 kPa	128 ms	0.21 kPa
③	800 mm	60 kPa	6.18 kPa	115 ms	0.76 kPa
④	600 mm	60 kPa	4.28 kPa	133 ms	0.71 kPa
⑤	600 mm	34.5 kPa	8.30 kPa	143 ms	0.54 kPa
⑥	600 mm	50 kPa	15.98 kPa	139 ms	0.56 kPa
⑦	500 mm	55 kPa	16.08 kPa	209 ms	0.51 kPa
⑧	500 mm	58 kPa	32.14 kPa	170 ms	1.46 kPa
⑨	500 mm	40.5 kPa	18.29 kPa	188 ms	0.66 kPa

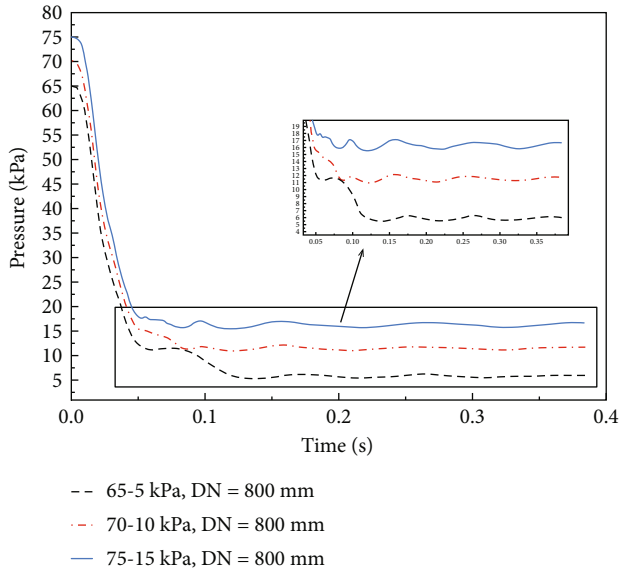

Figure 10: Rapid decompression test when DN = 800 mm.

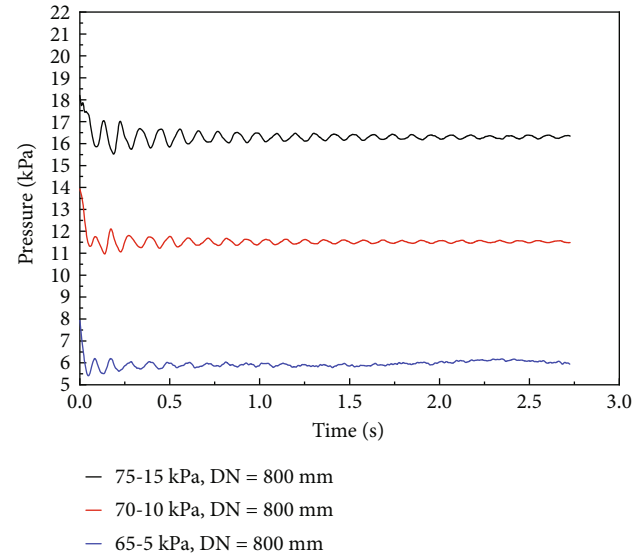

Figure 11: Rapid decompression and balancing process when DN = 800 mm.

experimental design. The pressure changes generated in the rapid decompression process and the impact of pressure oscillation on the cabin are collected. Table 2 shows the results of the rapid decompression test, including the main results of the rapid decompression equilibrium pressure of the two chambers, rapid decompression time, and extreme value of the oscillation wave generated.

Figure 10 shows the results of a rapid decompression test when DN = 800 mm. The rapid decompression time is within 100–200 ms. When the target pressure is almost reached, the oscillation phenomenon appears in the chamber. With the gradual stabilization of the pressure, the oscillation wave also gradually recovers. When the pipe diameter DN = 800 mm, $\Delta p_1 = \Delta p_2 = \Delta p_3 = 60$ kPa, oscillations with different amplitudes are generated, which are also related to the initial and target pressures of the rapid decompression. When the pressure of the low-pressure compartment is 65 kPa and the pressure of the negative pressure compartment is 5 kPa, the oscillation amplitude and the impact on the compartment are the largest.

As shown in Figure 11, after the rapid decompression reaches the target pressure, still residual waves appear in the process of pressure balance between the two chambers. The entire process requires more than 3 s before the two chambers can reach equilibrium. At this time, the residual waves still have an impact on the chambers. In the flow path of DN = 800 mm, the impact within 0–500 ms is the largest, and the oscillation amplitude is larger. With the consumption of energy, the pressure reduction system quickly recovers to the equilibrium state.

Figure 12 shows the results of the rapid decompression test when the pipe diameter is DN = 600 mm, where $\Delta p_1 = 60$ kPa, $\Delta p_2 = 34.5$ kPa, and $\Delta p_3 = 50$ kPa. After the pipe diameter is reduced, the oscillation wave generated during the rapid decompression process and the impact on the chamber are smaller. In the test with DN = 600 mm, the pressure difference varies in each test, and the oscillation waves generated are also different. When the pressure of the low-pressure chamber is 45.2 kPa and the pressure of the vacuum chamber is 7.56 kPa, although the initial and target pressures are both small, the pressure difference is also the smallest. Thus, the generated oscillation wave is relatively stable, and the impact on the chamber is the smallest. When the altitude chamber is 63.1 kPa and the vacuum

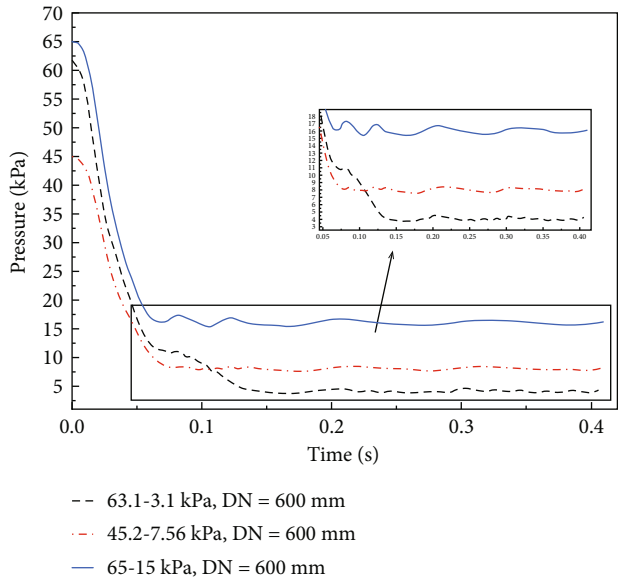

Figure 12: Rapid decompression test when DN = 600 mm.

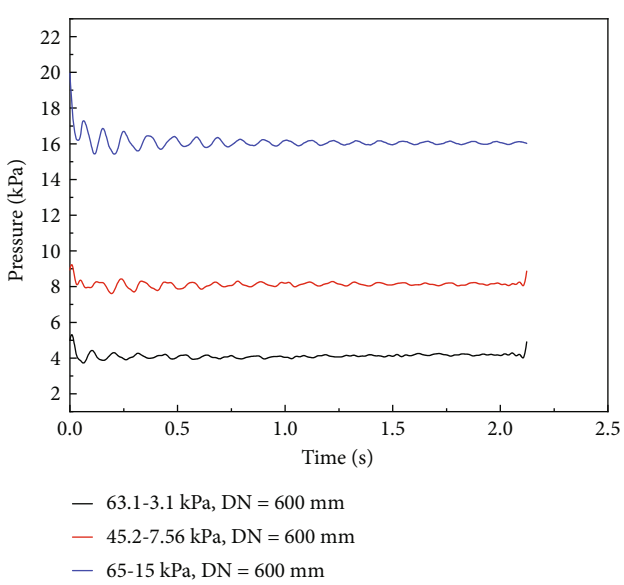

Figure 13: Rapid decompression and balancing process when DN = 600 mm.

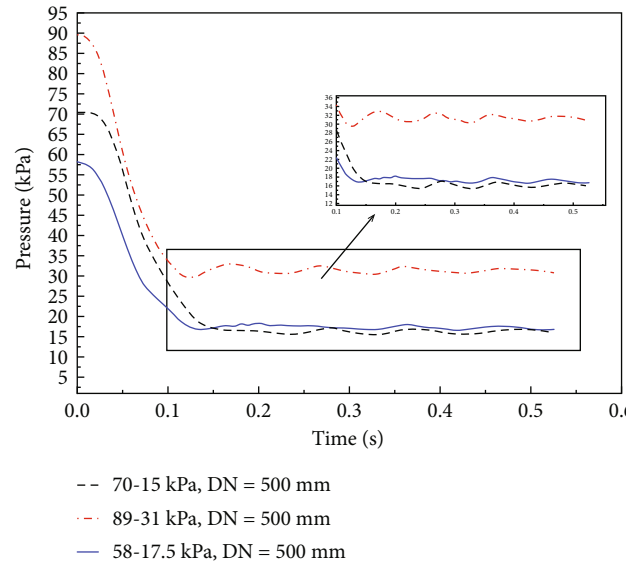

Figure 14: Rapid decompression test when DN = 500 mm.

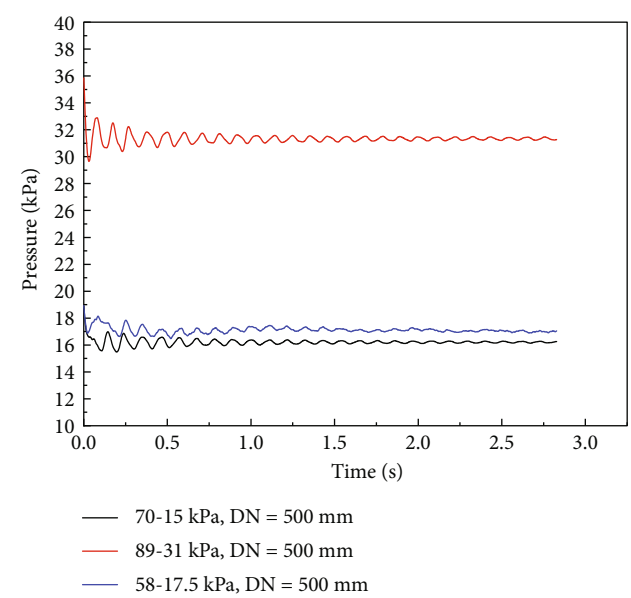

Figure 15: Rapid decompression and balancing process when DN = 500 mm.

chamber is 3.1 kPa, a large oscillation wave is also generated. At this time, when DN = 600 mm, the impact of the oscillation wave on the chamber is the largest.

As shown in Figure 13, when the pipe diameter DN = 600 mm, the residual wave generated after the rapid decompression reaches the target pressure. The maximum impact amount in the entire process is within 0–500 ms, and the impact on the chamber is the maximum. As the shock wave generated by the oscillation is absorbed by the inner wall, it gradually reaches the equilibrium state after 3 s, and the two chambers are connected when the pressure is rapidly reduced. Due to the large volume difference between the two chambers, although the test is conducted under the same pipe diameter, the difference between the initial and the target pressures of each test will make the time to finally reach equilibrium slightly different.

Figure 14 shows the results of the rapid decompression test when the pipe diameter DN = 500 mm, where $\Delta p_1 = 55$ kPa, $\Delta p_2 = 58$ kPa, and $\Delta p_3 = 40.5$ kPa. The oscillation wave generated by rapid decompression becomes smaller, and that generated when the pressure difference is 58 kPa is the largest. The initial pressure of the two chambers also becomes an important factor for the oscillation during rapid decompression. The change in the flow pipe diameter will also make the rapid decompression time longer and the speed reduced. Further, the oscillation generated will be

smaller than that caused by the oscillation of the large flow pipe diameter.

The action time of the residual wave will also be extended under the small flow pipe diameter after the rapid decompression reaches the target pressure. As shown in Figure 15, the oscillation wave remains large within 0–1 s, but the time to balance is as long as 3 s.

5. Conclusions

The characteristics of rapid decompression oscillation in an altitude chamber were analyzed in this study. Considering the variable cross-section pipeline that connects the altitude and vacuum chambers as the characteristic, the polynomial parameter expression of the rapid decompression system was established, and the oscillation phenomenon in the rapid decompression process was numerically simulated and analyzed. The following are the numerical simulation and test results.

By setting different pipe diameter and the initial pressure of the altitude and initial chambers, the test results indicate that different initial conditions produce different oscillation waves. (1) When DN = 800 mm, the test pressure difference is $\Delta p = 60$ kPa, and the initial pressures of the two chambers are different; the oscillation wave is also different. Further, the lower the pressure of the vacuum chamber, the higher the potential that the oscillation phenomenon occurs. Particularly, the maximum oscillation value reaches 0.76 kPa, and the rapid decompression time is 115 ms. (2) When DN = 600 mm, the pressure difference is not the same as the initial pressure. Moreover, the occurrence potential of the oscillation phenomenon is the highest under the test condition with the maximum pressure difference and lowest pressure in the altitude chamber. Specifically, the maximum oscillation value reaches 0.71 kPa, and the rapid decompression time is 133 ms. (3) When DN = 500 mm and when the pressure difference is different, the test conditions with the largest pressure difference have severe oscillation. Particularly, the maximum oscillation value reaches 1.46 kPa, and the rapid decompression time is 170 ms.

The three factors of the oscillation characteristics of the rapid decompression system are the size of the pipe diameter, pressure difference, and pressure of the vacuum chamber in that order. These three factors all affect the pressure oscillation and the rapid decompression time during the rapid decompression process. The rapid decompression time actually reflects the speed change during the rapid decompression process. The faster the speed change, the more likely the oscillation phenomenon will occur, causing chamber resonance and compromising equipment's safety and reliability.

Nomenclature

ΔR: Variation of the pipe radius
$R(z)$: Change rule of axial Z with radius R
v: Fluid kinematic viscosity coefficient
$\tilde{V}r$: Radial velocity of the pipe in a stable flow field
$\tilde{V}z$: Axial velocity of the pipe in a steady flow field
$\tilde{P}$: Pipeline pressure amplitude in a stable flow field
Re: Reynolds number
R_0: Pipe constant section radius
U_o: Average velocity of the pipeline in a steady flow field
$\tilde{\omega}$: Amplitude of the pipe velocity in a steady flow field
$\tilde{u}$: Velocity distribution of the pipe in a steady flow field
a: Polynomial coefficients about x in a steady flow field
$\bar{\omega}$: Velocity amplitude of the pipe in an oscillating flow field
$\bar{P}$: Amplitude of the pipeline pressure in an oscillating flow field
$\bar{u}$: Velocity distribution in an oscillating flow field
c: Polynomial coefficients of x in an oscillatory flow field.

Data Availability

The experimental data used to support the findings of this study are available from the corresponding author upon request.

Conflicts of Interest

The authors declare that they have no conflicts of interest.

Acknowledgments

The authors acknowledge the financial support from the fund of the Air Force Characteristic Medical Center (k21-0108-027). The authors would like to thank Air Force Characteristic Medical Center for providing the experimental platform.

References

[1] W. Shan-xiang, Q. Dong-chang, Z. Bin, C. Shan, G. U. Zhao, and X. Hua-jun, "Effects of rapid decompression on vision function as wearing soft contact lens," *Space Medicine & Medical Engineering*, vol. 24, no. 5, pp. 70–72, 2011.

[2] H. U. Hui-min, X. Hua-jun, D. Li, C. Shou-ping, Y. Chun-xin, and Q. Zhi-feng, "Effects of mild and moderate acute hypobaric hypoxia on manual performance," *Space Medicine & Medical Engineering*, vol. 21, no. 2, pp. 23–28, 2008.

[3] S. Wang, D. Qiang, B. Zang, S. Chen, Z. Gu, and H. Xiao, "Effects of high altitude hypobaria environment on visual function and contact lens transparency," *Space Medicine & MedicalEngineering*, vol. 24, no. 2, pp. 30–33, 2011.

[4] J. Lu, L. Li, and L. Chen, "Study on the decompression time of the hypobaric rapid decompression chamber," *International Journal of Heat and Technology*, vol. 33, no. 2, pp. 75–78, 2015.

[5] C. K. Allison, K. Revell, R. Sears, and N. A. Stanton, "Systems theoretic accident model and process (STAMP) safety modelling applied to an aircraft rapid decompression event," *Safety Science*, vol. 98, pp. 159–166, 2017.

[6] E. M. Roth, "Rapid (explosive) decompression emergencies in pressure-suited subjects. NASA CR-1223," *NASA contractor report*, National Aeronautics and Space Administration, NASA CR. United States, 1968.

[7] K. Urbanowicz, "Fast and accurate modelling of frictional transient pipe flow," *ZAMM-Journal of Applied Mathematics and Mechanics/Zeitschrift für Angewandte Mathematik und Mechanik*, vol. 98, no. 5, pp. 802–823, 2018.

[8] M. Karpenko, O. Prentkovskis, and S. Sukevicius, "Research on high-pressure hose with repairing fitting and influence on energy parameter of the hydraulic drive," *Eksploatacja i Niezawodnosc-Maintenance and Reliability*, vol. 24, no. 1, pp. 25–32, 2022.

[9] H. Ashley and G. Haviland, "Bending vibrations of a pipe line containing flowing fluid," *Journal Of Applied Mechanics-Transactions Of The Asme*, vol. 17, no. 3, pp. 229–232, 1950.

[10] H. Blackburn and R. Henderson, "Lock-in behavior in simulated vortex-induced vibration," *Experimental Thermal And Fluid Science*, vol. 12, no. 2, pp. 184–189, 1996.

[11] B. Chen, "Hybrid three-dimensional finite-difference and finite-element analysis of seismic wave induced fluid-structure interaction of a vertical cylinder," *Ocean Engineering*, vol. 25, no. 8, pp. 639–656, 1998.

[12] M. Ilgamov and R. Lukmanov, "Nonlinear vibrations of a pipeline under the action of pressure waves in fluid," in *Proceedings Of The Ninth (1999) International Offshore And Polar Engineering Conference*, pp. 145–152, Brest, France, 1999.

[13] C. Zuoyi, Y. Sun, Z. Y. Chen, and Y. Z. Sun, "The oscillating fluid mechanics method (OFMM) for studying oil film oscillation and dynamic characteristics of journal bearings," *Journal Of Tribology-Transactions Of The Asme*, vol. 118, no. 1, pp. 239–245, 1996.

[14] K. Urbanowicz, H. Duan, and A. Bergant, "Transient liquid flow in plastic pipes," *Strojniški vestnik – Journal of Mechanical Engineering*, vol. 66, no. 2, pp. 77–90, 2020.

[15] L. I. De-zhong, M. Ning, and L. U. Jian-hui, "Study on behavior of flow that induces vibration of pipeline on offshore platform," *Pipeline Technique and Equipment*, vol. 1, no. 3, pp. 8–10, 2006.

[16] D. Li, N. Mei, and J. Lu, "Study on behavior of flow that induces vibration of pipeline on offshore platform," *Pipeline Technique And Equipment*, vol. 46, pp. 5–7, 2006.

[17] J. B. V. Wanderley and C. A. Levi, "Validation of a finite difference method for the simulation of vortex-induced vibrations on a circular cylinder," *Ocean Engineering*, vol. 29, no. 4, pp. 445–460, 2002.

[18] M. P. P. Doussis and J. P. Denise, "Flutter of thin cylindrical shells conveying fluid," *Journal of Sound and Vibration*, vol. 20, no. 1, pp. 9–26, 1972.

[19] Y. Matsuzaki and Y. C. Fung, "Unsteady fluid dynamic forces on a simply-supported circular cylinder of finite length conveying a flow, with applications to stability analysis," *Journal of Sound and Vibration*, vol. 54, no. 3, pp. 317–330, 1977.

[20] R. W. Gregory and M. P. Paidoussis, "Unstable oscillation of tubular cantilevers conveying fluid II," *Experiments. Proceedings of the Royal Society of London. Series A. Mathematical and Physical Sciences*, vol. 293, no. 1435, pp. 528–542, 1966.

[21] F. Bourrieres, *The Auto-Oscillations of Real Jets in an Identical Medium by Auto-Folding*, Comptes Rendus Hebdomadaires Des Seances De L Academie Des Sciences, 1937.

[22] M. M. Bhatti, O. A. Bég, R. Ellahi, and T. Abbas, "Natural convection non-Newtonian EMHD dissipative flow through a microchannel containing a non-Darcy porous medium: homotopy perturbation method study," *Qualitative Theory of Dynamical Systems*, vol. 21, no. 4, p. 97, 2022.

[23] K. Jeong and K. Kim, "Free vibration of a circular cylindrical shell filled with bounded compressible fluid," *Journal of Sound and Vibration*, vol. 217, no. 2, pp. 197–221, 1998.

[24] Z. Liu, Y. Sun, and Y. Wu, "Vibration and stability of cylindrical shell conveying compressible fluid," *Chuan Bo Li Xue/Journal of Ship Mechanics*, vol. 4, no. 5, pp. 52–59, 2000.

[25] P. Liu, S. Kaewunruen, and B. Tang, "Dynamic pressure analysis of hemispherical shell vibrating in unbounded compressible fluid," *Applied Sciences-Basel*, vol. 8, no. 10, p. 1938, 2018.

[26] P. Liu, B. Tang, and S. Kaewunruen, "Vibration-induced pressures on a cylindrical structure surface in compressible fluid," *Applied Sciences-Basel*, vol. 9, no. 7, p. 1403, 2019.

[27] K. Jeong and K. Kim, "Hydroelastic vibration of a circular plate submerged in a bounded compressible fluid," *Journal of Sound and Vibration*, vol. 283, no. 1-2, pp. 153–172, 2005.

[28] V. Skrickij, D. Savitski, V. Ivanov, and P. Skačkauskas, "Investigation of cavitation process in monotube shock absorber," *International Journal of Automotive Technology*, vol. 19, no. 5, pp. 801–810, 2018.

[29] M. Massoudi and A. Vaidya, "Unsteady flows of inhomogeneous incompressible fluids," *International Journal of Non-Linear Mechanics*, vol. 46, no. 5, pp. 738–741, 2011.

[30] M. A. Imran, A. Sohail, and N. Shahid, "Exact solutions for oscillating motion of a second-grade fluid along an edge with mixed boundary conditions," *Chemical Engineering Communications*, vol. 199, no. 9, pp. 1085–1101, 2012.

[31] D. V. Kondratov, Y. N. Kondratova, and L. I. Mogilevich, "Oscillating laminar fluid flow in a cylindrical elastic pipe of annular cross-section," *Fluid Dynamics*, vol. 44, no. 4, pp. 528–539, 2009.

[32] B. K. Shivamoggi, "Hydrodynamic impulse in a compressible fluid," *Physics Letters A*, vol. 374, no. 47, pp. 4736–4740, 2010.

[33] Z. Chen, Y. Jing, and Y. Sun, "On the analysis of labyrinth seal flow induced vibration by oscillating fluid mechanics method," *Journal of Thermal Science*, vol. 3, no. 4, pp. 236–242, 1994.

[34] X. Liu, H. Xiao, B. Zang et al., "Evaluation of the physiological test in hypobaric chamber on new type oxygen supply system," *Chinese journal of Aerospace Medicine*, vol. 1, no. 2, pp. 91–97, 2012.

[35] J. H. Matuska and C. D. Taulbee, "Hypobaric test chamber design," *American Society of Mechanical Engineers, Pressure Vessels and Piping Division (Publication) PVP*, vol. 401, pp. 151–157, 2000.

[36] L. Hengli, C. Zuoyi, W. Pengfei, and W. Jue, "Analytical studies of fluid oscillating characteristics within a gas-liquid flow injector," in *Proceedings of the 1st International Conference on Engineering Thermophysics (ICET '99)*, pp. 323–329, Beijing (CN), 1999.